



Cite this: *J. Mater. Chem. C*, 2018, **6**, 4217

## Co-substitution in $\text{Ca}_{1-x}\text{Y}_x\text{Al}_{12-x}\text{Mg}_x\text{O}_{19}$ phosphors: local structure evolution, photoluminescence tuning and application for plant growth LEDs†

Yinjian Zheng,<sup>a</sup> Haiming Zhang,<sup>a</sup> Haoran Zhang,<sup>a</sup> Zhiguo Xia,<sup>b</sup> Yingliang Liu,<sup>b</sup> Maxim S. Molokeev<sup>c,d</sup> and Bingfu Lei<sup>b,\*</sup>

Herein,  $\text{Mn}^{4+}$ -activated  $\text{Ca}_{1-x}\text{Y}_x\text{Al}_{12-x}\text{Mg}_x\text{O}_{19}$  ( $x = 0-0.50$ ) solid solutions were prepared using a conventional high-temperature solid-state reaction. Crystal structure transformation *via* chemical co-substitution of  $\text{Y}^{3+}/\text{Mg}^{2+}$  for  $\text{Ca}^{2+}/\text{Al}^{3+}$  was investigated in detail. The optical properties of  $\text{Ca}_{1-x}\text{Y}_x\text{Al}_{12-x}\text{Mg}_x\text{O}_{19}$  ( $x = 0-0.50$ ) have been reported for the first time using a combination of techniques including structural refinement and luminescence measurements. Co-doping of Mg and Y cations within the  $\text{CaAl}_{12}\text{O}_{19}$  host in a controlled manner resulted in the as-prepared samples with red/far-red ratio-tunable luminescence properties. The emission bands well-matched with the absorption band of phytochrome. Interestingly, enhanced  $\text{Mn}^{4+}$  luminescence can be obtained upon the addition of  $\text{Mg}^{2+}$  and  $\text{Y}^{3+}$ . Unexpectedly, the quantum yields exhibit a slight change when  $x$  is in the range from 0.05 to 0.40; this indicates that these solid solutions have significant potential as lighting systems for plant growth.

Received 11th January 2018,  
Accepted 9th March 2018

DOI: 10.1039/c8tc00165k

rsc.li/materials-c

## Introduction

Light is an indispensable requirement for plant growth, which is not only an essential energy source for photosynthesis but also a power source for sprouting, blossoming, and fruiting as well as other morphogenesis of plants. In recent years, it has become increasingly cost effective to use artificial lights to assist plant growth.<sup>1-3</sup> Compared to conventional lighting technologies, including incandescent, halogen, and fluorescent lamps, phosphor-converted light-emitting diodes (LEDs) are promising candidates for artificial lighting for plant growth due to their low power consumption, reliability, long operation life, and luminescence tuning.<sup>4-6</sup> Especially, in terms of luminescence tuning, phosphor-converted LEDs have significant advantages as compared to the other abovementioned light sources. The spectrum power distribution of phosphor-converted LED grow lighting sources can be adjusted using various phosphors. Thus, LED grow lights can be used for plant growth to provide customized

light for a plant to grow and supplement sunlight to trigger specific growth and flowering. How to build LED grow lights? Prior to this, we need to understand the relationship between radiation and plants.<sup>7-12</sup> There are two representative processes related to the interaction between radiation and plants: photosynthesis and photo-morphogenesis. Photosynthesis is a process used by plants to convert light energy into chemical energy. The photosynthetic action spectrum (PAS) of plants shows that the characteristic absorption peaks for their chlorophylls are 450 nm blue emission and 660 nm red emission.<sup>13</sup> However, in the photo-morphogenetic photosystem, the existing pigments are phytochromes. The photo-morphogenetic responses mediated by phytochromes are usually related to the sensing of light quality through the red (R) to far-red (FR) ratio (R/FR). Photochromic pigments change their biological activity upon light absorption. In the case of a phytochrome, the ground state is Pr ('P' for phytochromes; 'r' for red light absorption). The absorbance maximum is a sharp peak at 650–670 nm. Once a red photon is absorbed, the pigment undergoes a rapid conformational change to form the Pfr state. Herein, fr indicates that now far-red (705–740 nm) and not red photon is preferentially absorbed. The phytochromes are sensitive to light in the red and far-red region of the visible spectrum. Thus, many flowering plants use them to regulate the time of flowering and set circadian rhythms. Phytochromes also regulate other responses including the germination of seeds, elongation of seedlings, the size, shape, and number of leaves, the synthesis of chlorophyll, and the straightening of the epicotyl or hypocotyl hook of dicot seedlings.

<sup>a</sup> Guangdong Provincial Engineering Technology Research Center for Optical Agricultural, College of Materials and Energy, South China Agricultural University, Guangzhou 510642, China. E-mail: tlei@scau.edu.cn

<sup>b</sup> School of Materials Sciences and Engineering, University of Science and Technology Beijing, Beijing 100083, China

<sup>c</sup> Laboratory of Crystal Physics, Kirensky Institute of Physics, Federal Research Center KSC SB RAS, Krasnoyarsk 660036, Russia

<sup>d</sup> Department of Physics, Far Eastern State Transport University, Khabarovsk, 680021, Russia

† Electronic supplementary information (ESI) available. See DOI: 10.1039/c8tc00165k

Conventional lighting sources (such as incandescent and fluorescent lamps) used for plant illumination suffer from the disadvantages of spectral mismatch with PAS. The spectrum of artificial lighting sources that matches with PAS is in the primary position for plant illumination to improve the photosynthetic efficiency. LEDs have been applied as a new lighting source in plant factories for plant-illumination since the 1980s due to their merits of higher conversion efficiency, smaller size, and longer lifetime; most important of all, the spectrum can be regulated by the distribution of the LED lighting sources in the factory used for plant illumination. However, the combination of red and blue LEDs applied in photosynthesis also has many disadvantages due to the narrowed emission spectrum width of the LEDs, resulting in the mismatch between the light sources and PAS of plants. Alternatively, phosphor-converted LEDs encapsulated with blue LED chips and broad blue and red-emitting multicomponent phosphors encapsulated with UV LED chips (or a blue-red dual-emitting single phase phosphor) can easily overcome this disadvantage, exhibiting superiorities in plant illumination.<sup>14,15</sup> Currently, some studies have been reported on phosphors applicable for LED grow lights to improve the photosynthetic efficiency. For example, Wang's group found that  $A_3MgSi_2O_8:Eu^{2+},Mn^{2+}$  (Ca, Ba, Sr) and  $Ca_3(PO_4)_2:Eu^{2+},Mn^{2+}$  were composed of simultaneous blue and red emission bands, which matched well with the photosynthesis absorption spectrum of chlorophylls.<sup>16–20</sup> The Guo group have developed a  $Li_2SrSiO_4:Ce^{3+},Pr^{3+}$  phosphor with blue, red, and NIR emission, which matches with the absorption spectrum of chlorophylls and carotenoids.<sup>21</sup> The Zheng group found that the emission of  $Mg_2Y_2Al_2Si_2O_{12}:Ce^{3+}$  ranged from 500 nm to 750 nm with the maximum located at 568 nm, which enhanced the red shift in the  $Ce^{3+}$  emission.<sup>22,23</sup> However, to date, only few studies have been reported on red and far red emission single-phase phosphors used for LED grow lights.<sup>24</sup> From the viewpoint of application, we have established and evaluated an approach to design tuneable R/FR ratio LED grow lights using suitable phosphors for plant growth and development.

The family of phosphors doped with  $Mn^{4+}$  ions has great potential applications in the commercial lighting industry. The classic phosphor  $3.5MgO \cdot 0.5MgF_2 \cdot GeO_2:Mn^{4+}$  has been widely applied as a colour correcting phosphor in fluorescent lamps to provide light for plant growth.<sup>25</sup> However, the raw materials of germanium are very costly. The red-emitting phosphor  $CaAl_{12}O_{19}:Mn^{4+}$  is regarded as a candidate of deep red-emitting phosphor in white LEDs due to its high brightness and low price.<sup>26</sup> Extensive research has been carried out to enhance the luminescence intensity of  $CaAl_{12}O_{19}:Mn^{4+}$  by mixing flux ( $CaF_2$ ,  $GeO_2$ ) or charge compensation ( $MgF_2$ ).<sup>27–30</sup> However, for successful application in LED grow lights, its luminescence properties still need to be further improved. The anion/cation substitution design strategy is an effective means to optimize the photoluminescence properties of phosphor materials. To date, many studies have been reported on phosphors, such as  $(Ca_{1-x}Li_x)(Al_{1-x}Si_{1+x})N_3:Eu^{2+}$ ,  $Bi_2(Ga,Al)_4O_9:Cr^{3+}$ ,  $Lu_{3-x}Y_xMgAl_3SiO_{12}:Ce^{3+}$ ,  $Ca_2(Al_{1-x}Mg_x)(Al_{1-x}Si_{1+x})O_7:Eu^{2+}$ ,  $La_5(Si_{2+x}B_{1-x})(O_{13-x}N_x):Ce^{3+}$ , and  $Ca_{2+x}La_{8-x}(SiO_4)_{6-x}(PO_4)_xO_2:Eu^{2+}$ , modified using anion/cation substitution.<sup>31–36</sup>

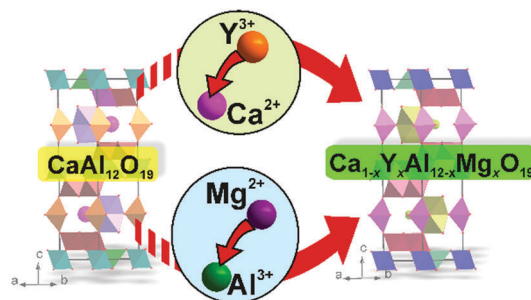


Fig. 1 A schematic of the construction of  $Ca_{1-x}Y_xAl_{12-x}Mg_xO_{19}$  from  $CaAl_{12}O_{19}$  via the co-substitution mechanism of  $Y^{3+}/Mg^{2+}$  for  $Ca^{2+}/Al^{3+}$ .

These results verify that co-substitution is a powerful strategy to discover phosphors with controlled/tuneable functional properties. This has stimulated us to experimentally use this strategy on the  $CaAl_{12}O_{19}:Mn^{4+}$  phosphor. In this study, the Ca, Al site co-substitution strategy was applied to the  $Ca_{1-x}Al_{12-x}Y_xMg_xO_{19}:Mn^{4+}$  solid solution phosphors (Fig. 1).

## Results and discussion

### Structure and phase purity

Rietveld refinement was performed using TOPAS 4.2.<sup>37</sup> Almost all the peaks were indexed using a hexagonal cell ( $P6_3/mmc$ ) with parameters close to those of  $CaAl_{12}O_{19}$  (hibonite-type crystals) besides small peaks, which can be described by the existence of small amounts of  $Al_2O_3$ ,  $MgAl_2O_4$ , and  $YAlO_3$  impurities.<sup>38</sup> There are five Al sites and one Ca site in the crystal structure (Fig. 2a). Fig. S1 (ESI<sup>†</sup>) shows the dependence of the average bond lengths and some particular bond lengths on the increasing  $x$ . It can be seen (Fig. 2b) that the average bond lengths  $d(Al1-O)_{aver}$ ,  $d(Al4-O)_{aver}$ , and  $d(Al5-O)_{aver}$  remain almost invariable upon increasing  $x$ ; thus, it can be speculated that Mg and Y ions do not prefer to occupy the sites Al1, Al4, and Al5. It should be noted that the  $Al5O_5$  trigonal bipyramid has an elongated form (Fig. 2a), and the two bond lengths  $d(Al5-O4)$  and  $d(Al5-O5)$  have also been investigated. It was found that  $d(Al5-O4)$  decreases but  $d(Al5-O5)$  increases with

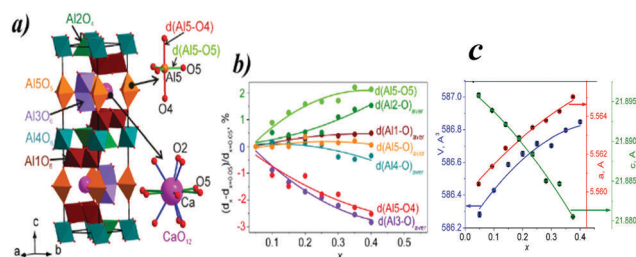


Fig. 2 The crystal structure of  $CaAl_{12}O_{19}$  (a) with the highlighted geometry of the  $Al5O_5$  and  $CaO_{12}$  polyhedra. The relative bond length deviation of all the  $d(Al-O)$  bonds per  $x$  value (b). The average bond lengths  $d(Al1-O)_{aver}$ ,  $d(Al4-O)_{aver}$ , and  $d(Al5-O)_{aver}$  are almost invariable upon increasing  $x$ , speculating the absence of Al/Mg or Al/Y substitution at the corresponding sites. (c) The cell parameters  $a$  (a) and  $c$  (b), and the cell volume (c) dependencies of  $(Ca_{1-x}Y_x)(Al_{12-x}Mg_x)O_{19}:Mn^{4+}$  per  $x$  value.

the increasing  $x$  (Fig. 2b). Moreover, the  $d(\text{Al2-O})_{\text{aver}}$  and  $d(\text{Al3-O})_{\text{aver}}$  lengths show noticeable changes, increasing and decreasing, respectively. Since Mg and Y ions are bigger than Al ion (for example, IR ( $\text{Al}^{3+}$ , CN = 6) = 0.535 Å, IR ( $\text{Mg}^{2+}$ , CN = 6) = 0.72 Å, and IR ( $\text{Y}^{3+}$ , CN = 6) = 0.9 Å), we cannot suggest that the Al3 site is occupied by  $\text{Mg}^{2+}$  or  $\text{Y}^{3+}$  ions. This shrinkage can be associated with the transformation mechanism of the whole structure, which leads to polyhedra deformation, and this mechanism has been discussed further. Thus, only the Al2 site can be occupied by  $\text{Mg}^{2+}/\text{Y}^{3+}$  ions, but since  $\text{Al2O}_4$  is tetrahedral and  $\text{Y}^{3+}$  cannot form this polyhedra, we can conclude that only  $\text{Mg}^{2+}$  can occupy the Al2 site. In this case,  $\text{Y}^{3+}$  ion should occupy the Ca site because this is the only site remaining accessible, and it does not matter that the average bond length of  $d(\text{Ca-O})_{\text{aver}}$  increases with  $x$  (Fig. S1f–h, ESI†). There are no ions in the structure that are larger than  $\text{Ca}^{2+}$  ion, and the reason for the increase in  $d(\text{Ca-O})_{\text{aver}}$  can also be associated with polyhedra deformation during the transformation mechanism.

The structural model for refinement was improved according to the abovementioned ideas. The sites of  $\text{Ca}^{2+}$  ion were occupied by  $\text{Y}^{3+}$  ions, and  $\text{Al}^{3+}$  ions at the Al2 sites were partly substituted by  $\text{Mg}^{2+}$  ions. The occupancies of  $\text{Y}^{3+}$  and  $\text{Mg}^{2+}$  at the Ca and Al sites were linearly interrelated to obtain zero sums of charges in the unit cell, and only one parameter of  $\text{Y}^{3+}$  occupancy was refined.  $\text{Mn}^{4+}$  ion was not used in the refinement due to its small concentration. The refinements were stable and provided low  $R$ -factors (Table 1, Fig. S2, ESI†). The coordinates of the atoms and main bond lengths are reported in Tables S1 and S2 (ESI†), respectively.

It is worth to discuss the transformation of the crystal structure under the substitution of  $\text{Ca}^{2+} \rightarrow \text{Y}^{3+}$  and  $\text{Al}^{3+} \rightarrow \text{Mg}^{2+}$ . The cell parameters  $a$  and  $c$  show diverse behaviour:  $a$  increases but  $c$  decreases upon increasing  $x$  (Fig. 2c). Since the cell volume is proportional to  $a^2$ , the cell volume also increases with  $x$  (Fig. 2c). The reason for the increase in  $a$  with  $x$  can be easily understood from Fig. 3a. The substitution of the  $\text{Al}^{3+}$  ion by the larger  $\text{Mg}^{2+}$  ion leads to the expansion of the  $(\text{Al2/Mg2})\text{O}_4$  tetrahedron and of course to the elongation of the cell parameter  $a$ . This expansion is one of the reasons why the  $d(\text{Ca-O5})$  bond length (Fig. 3c), which is

lying in the  $ab$ -plane, increases with  $x$  (Fig. 2a and Fig. S1h, ESI†) although  $\text{Ca}^{2+}$  ion is replaced by a smaller  $\text{Y}^{3+}$  ion. In addition, the bond length  $d(\text{Al5-O5})$  lies in the  $ab$ -plane (Fig. 2a) and also increases with  $x$  (Fig. 2b and 3c). Moreover, the expansion of the  $(\text{Al2/Mg2})\text{O}_4$  tetrahedra leads to the formation of alternate expanding and contracting layers along the  $c$ -axis because the space between two expanding layers with  $(\text{Al2/Mg2})\text{O}_4$  undergoes compression (Fig. 3b). Since the total length of the compressed layers in the  $c$  direction is larger than the length of the expanding layers, the compression overcomes stretching, and the  $c$  cell parameter decreases with  $x$ . This mechanism explains the decrease in the  $d(\text{Al5-O2})$  bond length because it is along the  $c$ -axis (Fig. 3c). However, the O2 ion, which is coordinated to  $\text{Ca}^{2+}$  ion, moves in two directions, and as a result, the  $d(\text{Ca-O2})$  bond length becomes bigger (Fig. 3c and Fig. S1g, ESI†).

Although the designed solid solution compounds possess the same hibonite structure, various chemical compositions will produce different crystal field environments for the doped activators; this further affects the luminescence properties of the as-prepared solid solution phosphors. In the present case, upon the progressive replacement of  $\text{Al}^{3+}$  and  $\text{Ca}^{2+}$  with  $\text{Mg}^{2+}$  and  $\text{Y}^{3+}$ , respectively, the color-tunable emission can be controlled by changing the chemical compositions of the solid solution.<sup>39</sup>

### SEM images

The particle morphology of  $(\text{Ca}_{1-x}\text{Y}_x)(\text{Al}_{12-x}\text{Mg}_x)\text{O}_{19}:\text{Mn}^{4+}$  was studied using SEM. Fig. 4 shows the SEM images of the selected  $(\text{Ca}_{1-x}\text{Y}_x)(\text{Al}_{12-x}\text{Mg}_x)\text{O}_{19}:\text{Mn}^{4+}$  ( $x = 0, 0.1, 0.2, 0.3, 0.4,$  and  $0.5$ ) phosphors. Since a high temperature is required in the powder calcination step and the samples have to be milled thoroughly prior to the SEM measurements, it can be found in Fig. 4 that all the powder products have an irregular morphology in the micrometer range, and their surface morphology does not change significantly depending on the different values of  $x$ . The as-prepared phosphors contain particles with different sizes in the range of 1–30  $\mu\text{m}$ . These relatively large particles mainly consist of aggregated grains with diameter 5–10  $\mu\text{m}$ . To meet the requirements for advanced plant grow applications, it is necessary to reduce aggregation by further synthesis optimization.

**Table 1** The main parameters of processing and refinement of the  $(\text{CaAl})_{1-x}(\text{YMg})_x\text{Al}_{11}\text{O}_{19}:\text{Mn}^{4+}$  samples

$x$	Refined $x$	Space group	Cell parameters (Å)	Volume (Å <sup>3</sup> )	$R_{\text{wp}}, R_{\text{p}}, R_{\text{B}}$ (%)	$\chi^2$
0.05	0.057 (5)	$P6_3/mmc$	$a = 5.56042$ (7) $c = 21.8958$ (2)	586.283 (15)	10.24, 7.71, 5.38	1.58
0.10	0.053 (4)	$P6_3/mmc$	$a = 5.56136$ (3) $c = 21.89389$ (12)	586.428 (6)	9.46, 7.15, 3.88	1.46
0.15	0.088 (5)	$P6_3/mmc$	$a = 5.56233$ (5) $c = 21.8921$ (2)	586.587 (12)	9.62, 7.27, 3.79	1.49
0.20	0.131 (5)	$P6_3/mmc$	$a = 5.56288$ (6) $c = 21.8904$ (3)	586.654 (15)	9.76, 7.35, 4.63	1.53
0.25	0.145 (4)	$P6_3/mmc$	$a = 5.56241$ (5) $c = 21.8884$ (2)	586.715 (13)	9.46, 7.16, 3.98	1.49
0.30	0.173 (4)	$P6_3/mmc$	$a = 5.56379$ (3) $c = 21.8850$ (2)	586.703 (8)	9.09, 6.87, 3.87	1.43
0.35	0.164 (5)	$P6_3/mmc$	$a = 5.56427$ (4) $c = 21.8847$ (2)	586.796 (9)	8.87, 6.82, 3.07	1.39
0.40	0.211 (5)	$P6_3/mmc$	$a = 5.56504$ (7) $c = 21.8805$ (2)	586.85 (1)	9.33, 7.16, 3.25	1.48

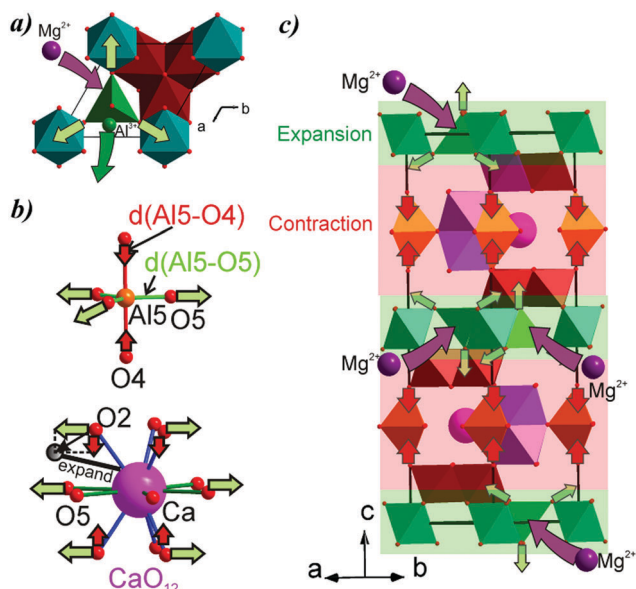


Fig. 3 The mechanism of elongation along the *a*- and *b*-axis upon increasing *x* in  $(\text{Ca}_{1-x}\text{Y}_x)(\text{Al}_{12-x}\text{Mg}_x)\text{O}_{19}:\text{Mn}^{4+}$  is associated with the expansion of the  $(\text{Al}_2/\text{Mg}_2)\text{O}_4$  tetrahedron due to the substitution of a small  $\text{Al}^{3+}$  ion by the larger  $\text{Mg}^{2+}$  ion (a). The mechanism of contraction along the *c*-axis is associated with the compression of red layers between the two expanding (green) layers with  $(\text{Al}_2/\text{Mg}_2)\text{O}_4$  polyhedra (b). These two mechanisms explain the increase in  $d(\text{Al5}-\text{O5})$  and decrease in  $d(\text{Al5}-\text{O4})$  bond lengths in the  $\text{Al5O}_5$  trigonal pyramid and increase in all the  $d(\text{Ca}-\text{O})$  bond lengths (c).

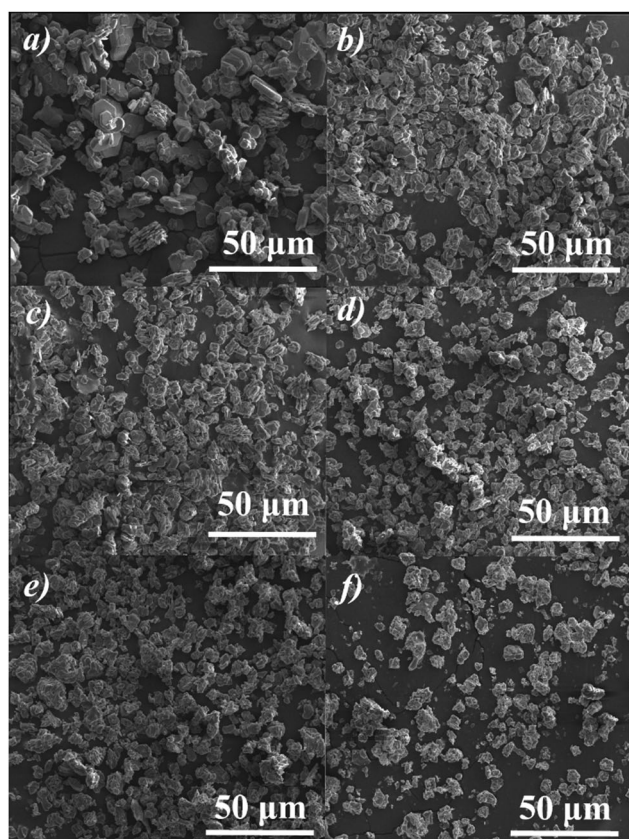


Fig. 4 The SEM images of  $(\text{Ca}_{1-x}\text{Y}_x)(\text{Al}_{12-x}\text{Mg}_x)\text{O}_{19}:\text{Mn}^{4+}$  with different *x* values, *x* = 0 (a), *x* = 0.1 (b), *x* = 0.2 (c), *x* = 0.3 (d), *x* = 0.4 (e), and *x* = 0.5 (f).

### Photoluminescence properties

The DR spectrum of  $\text{CaAl}_{12}\text{O}_{19}:\text{Mn}^{4+}$  is shown in Fig. 5a. The sample shows a strong decrease in the reflection in the UV range. In addition, it shows a strong absorption band in the wavelength range 400–550 nm, which is in good agreement with the pink color observed for the  $\text{CaAl}_{12}\text{O}_{19}:\text{Mn}^{4+}$  phosphor. The photoluminescence excitation (PLE) and emission spectra (PL) of the  $\text{CaAl}_{12}\text{O}_{19}:\text{Mn}^{4+}$  phosphor at room temperature are displayed in Fig. 5b and c, respectively. The PLE spectrum monitored at about 655 nm covers a very broad spectral region, which includes three main bands. As shown in Fig. 5b, the first band ( $\sim 320$  nm) can be assigned to the spin-allowed  ${}^4\text{A}_2 \rightarrow {}^4\text{T}_1$  ( $4\text{F}$ ) transition of  $\text{Mn}^{4+}$  (partly due to the charge transfer of  $\text{O}^{2-}-\text{Mn}^{4+}$ ), and the two remaining bands can be attributed to the spin and parity forbidden transitions,  ${}^4\text{A}_2 \rightarrow {}^4\text{T}_1$  transition of  $\text{Mn}^{4+}$  ( $\sim 394$  nm) and  ${}^4\text{A}_2 \rightarrow {}^4\text{T}_2$  transition of  $\text{Mn}^{4+}$  ( $\sim 461$  nm), respectively. The emission spectrum of  $\text{Mn}^{4+}$ -doped  $\text{CaAl}_{12}\text{O}_{19}$  is also shown in Fig. 5c. The phosphor shows emissions in the wavelength range between 600 nm and 750 nm with the maximum located at 655 nm in the visible-light region. The main peaks correspond to the transition from the lowest excited level of  ${}^2\text{E}$  to the ground state  ${}^4\text{A}_2$  of  $\text{Mn}^{4+}$  ion.<sup>40</sup>

Fig. 6 shows the PLE and PL spectra of the  $(\text{Ca}_{1-x}\text{Y}_x)(\text{Al}_{12-x}\text{Mg}_x)\text{O}_{19}:\text{Mn}^{4+}$  phosphors as a function of *x*. The position of the excitation band is independent of the *x* value. All the  $(\text{Ca}_{1-x}\text{Y}_x)(\text{Al}_{12-x}\text{Mg}_x)\text{O}_{19}:\text{Mn}^{4+}$  (*x* = 0–0.50) samples have excellent excitation spectral profiles, which match well with those of commercial LEDs such as GaN (emission wavelength around 460 nm), InGaN (400 nm), and AlInGaN (320 nm). Fig. 6b presents the emission spectra ( $\lambda_{\text{ex}} = 320$  nm) as a function of *x* for the  $(\text{Ca}_{1-x}\text{Y}_x)(\text{Al}_{12-x}\text{Mg}_x)\text{O}_{19}:\text{Mn}^{4+}$  samples. The PL spectra are similar to the spectrum of  $\text{Mn}^{4+}$  ions in the pure  $\text{CaAl}_{12}\text{O}_{19}$  phase sample with *x*  $\leq$  0.10. According to previous studies, the emission band between 620 nm and 650 nm is due to the anti-Stokes vibronic sidebands associated with the excited state  ${}^2\text{E}$  of  $\text{Mn}^{4+}$ . In addition, the emission band in the region of 660–720 nm is due to lattice vibronic transitions of  $\text{Mn}^{4+}$ . The strong emission band between 650 and 660 nm can be attributed to the  ${}^2\text{E}-{}^4\text{A}_2$  transition of  $\text{Mn}^{4+}$ . When *x* = 0.15, a new peak

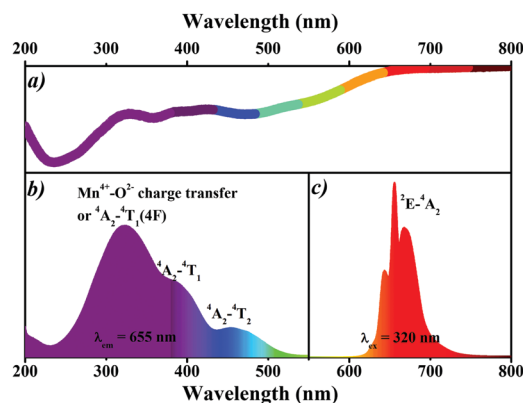


Fig. 5 The UV-vis DR spectrum (a), PLE spectrum (b), and PL spectrum (c) of the  $\text{CaAl}_{12}\text{O}_{19}:\text{Mn}^{4+}$  material.

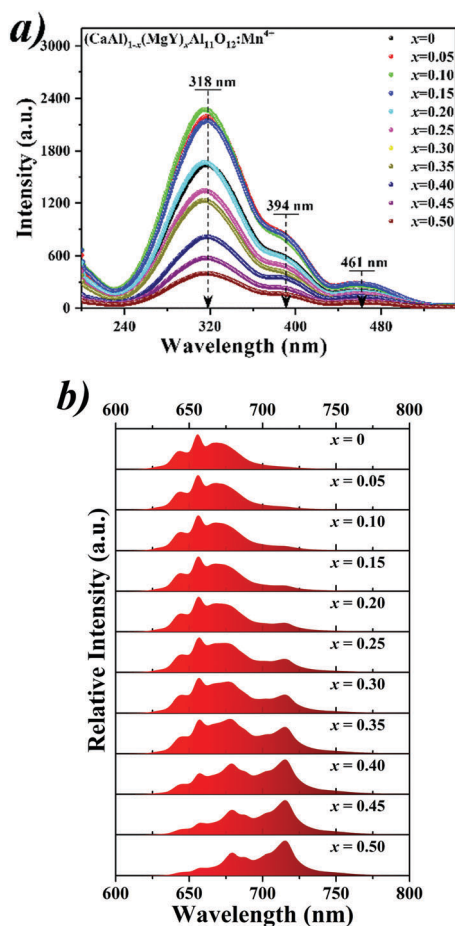


Fig. 6 The PLE (a) and PL (b) spectra of the  $(\text{Ca}_{1-x}\text{Y}_x)(\text{Al}_{12-x}\text{Mg}_x)\text{O}_{19}:\text{Mn}^{4+}$  ( $x = 0-0.50$ ) samples as a function of  $x$ .

emerges at 715 nm, which is not observed in the emission spectrum of  $\text{Mn}^{4+}$  in the pure phase of  $\text{CaAl}_{12}\text{O}_{19}$ . This result suggests that  $\text{Mn}^{4+}$  ions are located in a different phase. In the next sections, we have discussed this in more detail.

As shown in Fig. S2 (ESI<sup>†</sup>) and Table 2, some impurity phases, such as  $\text{Al}_2\text{O}_3$ ,  $\text{YAlO}_3$ , and  $\text{MgAl}_2\text{O}_4$ , grow as the value of  $x$  increases. On the basis of the study of the related literature, no evidence of  $\text{Mn}^{4+}$  ions in the  $\text{MgAl}_2\text{O}_4$  phase was observed.<sup>41</sup> That is, the emerging emission is probably due to the transition of  $\text{Mn}^{4+}$  in  $\text{Al}_2\text{O}_3$  and  $\text{YAlO}_3$ . The spectroscopic studies of  $\text{Mn}^{4+}$  ions in  $\text{YAlO}_3$ , performed by Noginov *et al.* showed that the luminescence spectra of  $\text{YAlO}_3:\text{Mn}^{4+}$  consisted of several emission peaks in the range from 670 to 750 nm (four major emission peaks corresponding to 680, 687, 702, and 715 nm).<sup>42</sup>  $\text{YAlO}_3:\text{Mn}^{4+}$  has been evaluated as a potential material for holographic recording, optical data storage, and thermoluminescence dosimetry.<sup>43</sup> Jovanik has reported that  $\text{Al}_2\text{O}_3:\text{Mn}^{4+}$  exhibits a red emission band from 670 to 690 nm. In addition, the emission maximum peaked at 678 nm.<sup>44</sup> However, there are no studies suggesting that  $\text{YAlO}_3:\text{Mn}^{4+}$  and  $\text{Al}_2\text{O}_3:\text{Mn}^{4+}$  have potential applications as phosphors in light-emitting diodes for modulating plant growth. An optical spectroscopy study revealed that the  $(\text{Ca}_{1-x}\text{Y}_x)(\text{Al}_{12-x}\text{Mg}_x)\text{O}_{19}:\text{Mn}^{4+}$  solid solution gave rise to the same spectra as that of the physically mixed bulk phosphors of  $\text{Al}_2\text{O}_3:\text{Mn}^{4+}$ ,  $\text{YAlO}_3:\text{Mn}^{4+}$ ,

Table 2 The component contents of the  $(\text{CaAl})_{1-x}(\text{YMg})_x\text{Al}_{11}\text{O}_{19}:\text{Mn}^{4+}$  samples

Phase	$\text{CaAl}_{12}\text{O}_{19}$	$\text{Al}_2\text{O}_3$	$\text{YAlO}_3$	$\text{MgAl}_2\text{O}_4$
0.05	99.0(1)%	1.0(1)%	—	—
0.10	97.8(1)%	1.4(1)%	0.8(1)%	—
0.15	96.6(1)%	2.3(1)%	1.1(1)%	—
0.20	93.4(3)%	3.5(1)%	1.6(1)%	1.5(3)%
0.25	91.2(2)%	4.7(1)%	2.1(1)%	2.0(1)%
0.30	89.1(2)%	5.8(1)%	2.5(1)%	2.6(1)%
0.35	85.5(2)%	7.8(1)%	3.1(1)%	3.6(1)%
0.40	81.7(3)%	9.9(2)%	3.8(1)%	4.6(1)%

and  $\text{CaAl}_{12}\text{O}_{19}:\text{Mn}^{4+}$ . In some studies, similar phenomenon has been found by adjusting the cation composition of the phosphors. These studies show that the as-prepared composite compounds may reveal additional properties due to some synergistic effects, which are not present in the individual compounds. It is notable that in the cases where  $\text{Mn}^{4+}$  photoluminescence enhancement occurs, there are impurity phases co-existing with the dominant phase such as  $\text{SrMgAl}_x\text{O}_y:\text{Mn}^{4+}$ , where  $\text{SrMgAl}_{10}\text{O}_{17}:\text{Mn}^{4+}$  and  $\text{Al}_2\text{O}_3:\text{Mn}^{4+}$  are co-precipitated as the aluminium content  $x$  increases. The emissions of  $\text{SrMgAl}_{10}\text{O}_{17}:\text{Mn}^{4+}$  and  $\text{Al}_2\text{O}_3:\text{Mn}^{4+}$  can be intensified by 2.6 and 222 times, respectively. However, the contribution of the co-existing phases to the enhancement of the photoluminescence has rarely been reported. Recently, Xia *et al.* have reported an isostructural solid solution of  $(\text{CaMg})_x(\text{NaSc})_{1-x}\text{Si}_2\text{O}_6$  in which cation nano-segregation leads to the presence of two dilute  $\text{Eu}^{2+}$  centers.<sup>45</sup> The distinct nano-domains of  $(\text{CaMg})\text{Si}_2\text{O}_6$  and  $(\text{NaSc})\text{Si}_2\text{O}_6$  contain a proportional number of  $\text{Eu}^{2+}$  ions with unique, independent spectroscopic signatures. In the present investigation, we believe that cation substitution/segregation leads to remarkable spectroscopic properties of  $(\text{Ca}_{1-x}\text{Y}_x)(\text{Al}_{12-x}\text{Mg}_x)\text{O}_{19}:\text{Mn}^{4+}$ .<sup>46,47</sup> The  $\text{Al}_2\text{O}_3:\text{Mn}^{4+}$ ,  $\text{YAlO}_3:\text{Mn}^{4+}$  and  $\text{CaAl}_{12}\text{O}_{19}:\text{Mn}^{4+}$  domains in the solid solution have significant advantages for tuning of photoluminescence when compared with a physical mixture. Moreover, the quantum yields of the  $(\text{Ca}_{1-x}\text{Y}_x)(\text{Al}_{12-x}\text{Mg}_x)\text{O}_{19}:\text{Mn}^{4+}$  composite phosphors are significantly enhanced and have been discussed in the next section.

Fig. 7a shows the normalized PL spectra of  $(\text{Ca}_{1-x}\text{Y}_x)(\text{Al}_{12-x}\text{Mg}_x)\text{O}_{19}:\text{Mn}^{4+}$ . We can clearly see that with an increase in the number of incorporated Y-Mg pairs, the emission band widens, and the emission peaks around 678 nm and 715 nm gradually increase. In other words, the far-red component increases with  $x$  in  $(\text{Ca}_{1-x}\text{Y}_x)(\text{Al}_{12-x}\text{Mg}_x)\text{O}_{19}:\text{Mn}^{4+}$ . Thus, the  $(\text{Ca}_{1-x}\text{Y}_x)(\text{Al}_{12-x}\text{Mg}_x)\text{O}_{19}:\text{Mn}^{4+}$  phosphors have the capability of controlling the spectral composition. Fig. 7b shows the integrated red (600–700 nm) and far-red (700–800 nm) PL intensities of the  $(\text{Ca}_{1-x}\text{Y}_x)(\text{Al}_{12-x}\text{Mg}_x)\text{O}_{19}:\text{Mn}^{4+}$  samples with various  $x$  values. It is clearly observed that the integrated intensity of the far-red emission (700–800 nm) continuously increases with an increase in the  $x$  value. The integrated intensity of the red emission (600–700 nm) increases gradually upon increasing the  $x$  content and begins to fall after reaching the maximum at  $x = 0.10$ . This enhancement is largely due to the incorporation of  $\text{Mg}^{2+}$  into the lattice and the replacement of the  $\text{Mn}^{4+}-\text{Mn}^{4+}$  neighbours by the  $\text{Mn}^{4+}-\text{Mg}^{2+}$  pairs. Fig. 7c shows the absorption spectra of the phytochrome. Compared to the absorption spectra of the

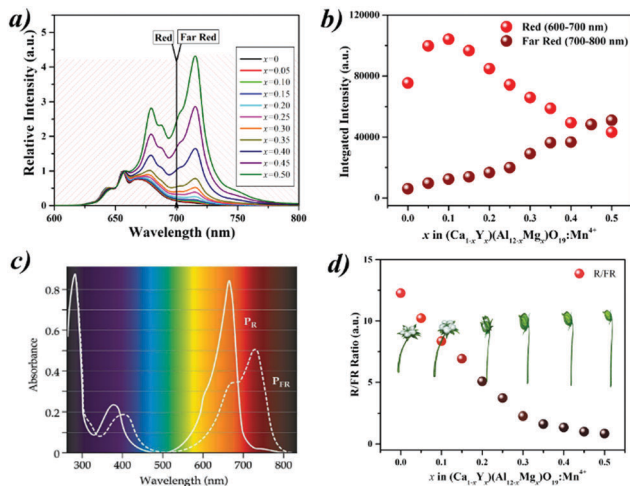


Fig. 7 The PL spectra of  $(\text{Ca}_{1-x}\text{Y}_x)(\text{Al}_{12-x}\text{Mg}_x)\text{O}_{19}:\text{Mn}^{4+}$  normalized at the emission peak intensity at 655 nm (a). The integrated red (600–700 nm) and far-red (700–800 nm) PL intensities of the  $(\text{Ca}_{1-x}\text{Y}_x)(\text{Al}_{12-x}\text{Mg}_x)\text{O}_{19}:\text{Mn}^{4+}$  samples (b). The absorption spectra of phytochrome (c). The relationships of  $x$  versus the R/FR ratio in the  $(\text{Ca}_{1-x}\text{Y}_x)(\text{Al}_{12-x}\text{Mg}_x)\text{O}_{19}:\text{Mn}^{4+}$  samples (d).

phytochromes  $\text{P}_R$  and  $\text{P}_{FR}$  in plants, the PL spectra of the  $(\text{Ca}_{1-x}\text{Y}_x)(\text{Al}_{12-x}\text{Mg}_x)\text{O}_{19}:\text{Mn}^{4+}$  phosphors overlap with the absorption of phytochrome. The emission light can match well with plant photoreceptors to offer ideal production and affect plant morphology. Fig. 7d shows that the ratio of the red and far-red emission intensities can be tuned properly by adjusting the  $x$  value in  $(\text{Ca}_{1-x}\text{Y}_x)(\text{Al}_{12-x}\text{Mg}_x)\text{O}_{19}:\text{Mn}^{4+}$ . The ratio of the red and far-red emission intensities provides important spatial and seasonal information of plants. The lower R/FR ratio leads to pronounced elongation growth and delayed flowering, elevating the leaves towards unfiltered daylight and promoting the seed set. According to this principle, it is easy to design phosphor-converted plant growth LEDs with different R/FR ratios, which are useful for controlling the plant morphology.

### Fluorescence lifetime

Fig. 8a and b exhibit the decay curves of  $(\text{Ca}_{1-x}\text{Y}_x)(\text{Al}_{12-x}\text{Mg}_x)\text{O}_{19}:\text{Mn}^{4+}$  under excitation at 320 nm. The average lifetime was used to characterize the effective decay process, which could be obtained directly using a FLS920 spectrofluorimeter with its software, as given in Fig. 8c and d. The average lifetimes monitored at 655 nm were approximately 1.042, 1.119, 1.080, 1.058, 1.055, 1.047, 1.050, 1.077, 1.094, 1.155, and 1.299 ms when the  $x$  value in the host corresponded to  $x = 0, 0.05, 0.10, 0.15, 0.20, 0.25, 0.30, 0.35, 0.40, 0.45,$  and  $0.50$ , respectively. The lifetimes of  $(\text{Ca}_{1-x}\text{Y}_x)(\text{Al}_{12-x}\text{Mg}_x)\text{O}_{19}:\text{Mn}^{4+}$  ( $x > 0$ ) lie between 1.047 and 1.299 ms, and it is longer than 1.042 ms observed for the  $\text{CaAl}_{12}\text{O}_{19}:\text{Mn}^{4+}$  ( $x = 0$ ) sample. Elongation of the lifetime is possible because of the reduced content of  $\text{Mn}^{4+}-\text{Mn}^{4+}$  pairs due to the formation of  $\text{Mg}^{2+}-\text{Mn}^{4+}$ . Fig. 8b shows the decay curves monitored at 715 nm. As shown in Fig. 8d, the obtained lifetimes monitored at 715 nm increase from 1.116 to 2.731 ms, corresponding to  $x = 0.15-0.50$ . To the best of our knowledge, the lifetime usually decreases because of faster radiative energy

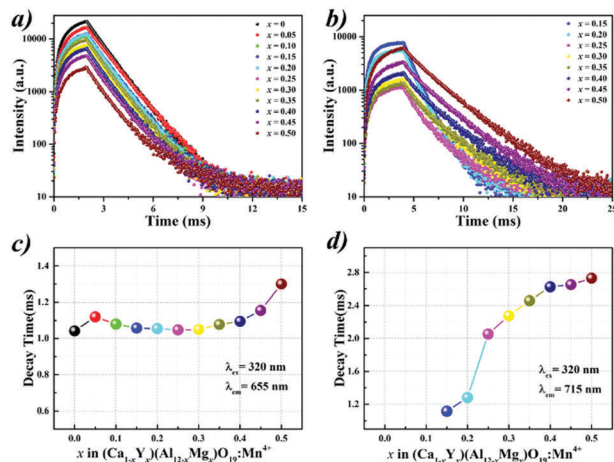


Fig. 8 The decay curves of the  $(\text{Ca}_{1-x}\text{Y}_x)(\text{Al}_{12-x}\text{Mg}_x)\text{O}_{19}:\text{Mn}^{4+}$  phosphors monitored at 656 nm (a) and 715 nm (b). The fluorescence lifetimes of the  $(\text{Ca}_{1-x}\text{Y}_x)(\text{Al}_{12-x}\text{Mg}_x)\text{O}_{19}:\text{Mn}^{4+}$  phosphors monitored at 656 nm (c) and 715 nm (d).

transfer, with the terminal step ending at a defect or killer site. However, the gradual increase in the average lifetimes implies the low energy transfer probability among  $\text{Mn}^{4+}$  ions. This co-substitution strategy ( $\text{Ca}^{2+} \rightarrow \text{Y}^{3+}$ ,  $\text{Al}^{3+} \rightarrow \text{Mg}^{2+}$ ) demonstrates remarkable performance improvement in the photoluminescence and also affects the non-radioactive processes such as the photoluminescence decay behaviour.

### Quantum efficiency

Quantum yield is one of the most important parameters for measuring phosphor performance.<sup>27,48</sup> The absolute quantum yield ( $\eta$ ) was measured using a FLS920 spectrofluorimeter equipped with an integrating sphere and calculated as follows:  $\eta = \int L_d / (\int E_w - \int E_d)$ , where  $\eta$  is the absolute quantum yield,  $L_d$  is the complete emission spectrum,  $E_d$  is the excitation spectrum for exciting the sample, and  $E_w$  is the emission spectrum of the excitation light obtained with the equipment-blank sample, *i.e.* without the  $(\text{Ca}_{1-x}\text{Y}_x)(\text{Al}_{12-x}\text{Mg}_x)\text{O}_{19}:\text{Mn}^{4+}$  sample. The absolute quantum yield of the  $(\text{Ca}_{1-x}\text{Y}_x)(\text{Al}_{12-x}\text{Mg}_x)\text{O}_{19}:\text{Mn}^{4+}$  samples under 320 nm wavelength excitation is shown in Fig. 9. The absolute quantum yield increases upon increasing the  $x$  value in  $(\text{Ca}_{1-x}\text{Y}_x)(\text{Al}_{12-x}\text{Mg}_x)\text{O}_{19}:\text{Mn}^{4+}$ . The absolute quantum yields for all the co-substitution samples are higher than that of the  $\text{CaAl}_{12}\text{O}_{19}:\text{Mn}^{4+}$  ( $x = 0$ ) sample. The absolute quantum yields change slightly with the  $x$  value in the range of 0.05–0.40. The quantum efficiency can be further improved by optimizing the synthesis procedure such as by adding flux. These phosphors have potential applications in the field of white LEDs with warm white light and artificial lighting, especially LED plant growth lighting. This is because the co-substitution series of phosphors matches well with the absorption of phytochrome.

### LED applications

Typical  $\text{Ca}_{1-x}\text{Y}_x\text{Al}_{12-x}\text{Mg}_x\text{O}_{19}:\text{Mn}^{4+}$  ( $x = 0, 0.10, 0.40$ ) phosphors were dispersed in silicon resin and coated onto UV LED chips ( $\lambda = 365$  nm). Fig. 10 shows the typical electroluminescence

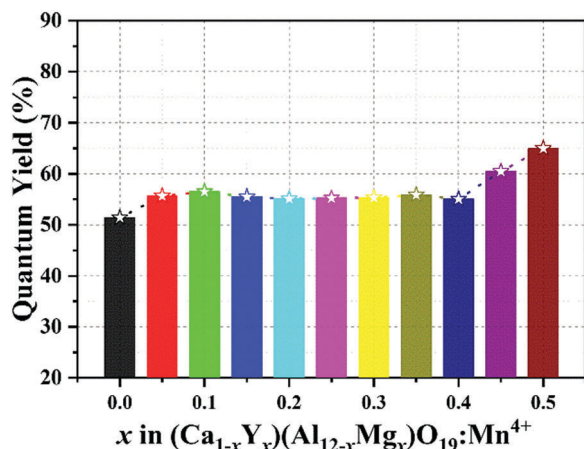


Fig. 9 The quantum efficiency of  $(\text{Ca}_{1-x}\text{Y}_x)(\text{Al}_{12-x}\text{Mg}_x)\text{O}_{19}:\text{Mn}^{4+}$  ( $x = 0-0.50$ ) upon excitation at 320 nm.

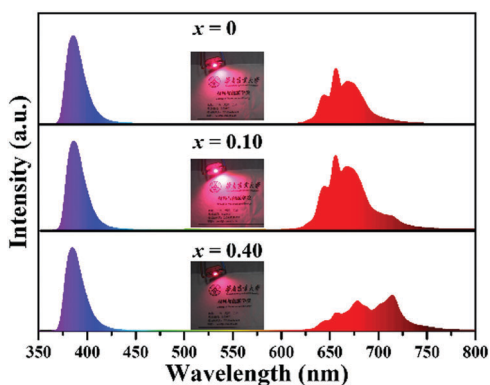


Fig. 10 The electroluminescence spectra of the phosphor-coated LEDs composed of a 365 nm UV chip and the typical  $\text{Ca}_{1-x}\text{Y}_x\text{Al}_{12-x}\text{Mg}_x\text{O}_{19}:\text{Mn}^{4+}$  ( $x = 0, 0.10,$  and  $0.40$ ) phosphors. The insets show the images of the as-fabricated LEDs in operation under a current of 20 mA and a bias voltage of 3 V.

spectra and images of the fabricated LEDs driven at a 20 mA current. As seen, phosphor-coated LEDs with various red/far red emission spectra were obtained. These results demonstrate that the  $\text{Ca}_{1-x}\text{Y}_x\text{Al}_{12-x}\text{Mg}_x\text{O}_{19}:\text{Mn}^{4+}$  phosphors have strong potential applications in the development of advanced plant grow LEDs.

Green-leaf pak-choi, red-leaf pak-choi, and flowering Chinese cabbage were used as plant models to study the photosynthesis and bio-active metabolism of plants, and cucumber seeding was used as a model to investigate how different R:FR ratios affect the plant germination and morphology. Overall, the different treatments have different results in the cultivate plants. In general, a higher-ratio of red light is helpful for photosynthesis, the accumulation of bio-active compounds, and an increase in biomass; a higher-ratio of infrared light has an opposite effect. For a detailed description, see the ESI.†

## Experimental

### Materials and preparation

The  $\text{Ca}_{1-x}\text{Y}_x\text{Al}_{12-x}\text{Mg}_x\text{O}_{19}:\text{Mn}^{4+}$  ( $x = 0, 0.05, 0.10, 0.15, 0.20, 0.25, 0.30, 0.35, 0.40, 0.45,$  and  $0.50$ ) solid-solution

phosphors were prepared using a conventional high-temperature solid-state method. The high purity  $\text{CaCO}_3$  (>99.9%),  $\text{Y}_2\text{O}_3$  (>99.99%),  $\text{Al}_2\text{O}_3$  (>99.9%),  $\text{MgO}$  (>99%), and  $\text{MnCO}_3$  (>99%) were used as the starting materials. The stoichiometric amounts of  $\text{CaCO}_3$ ,  $\text{Y}_2\text{O}_3$ ,  $\text{Al}_2\text{O}_3$ ,  $\text{MgO}$ , and  $\text{MnCO}_3$  were added and ground homogeneously with suitable amounts of ethanol using an agate mortar until the mixtures were almost dry. The mixtures of these materials were first heated at 120 °C for 2 h in an oven to release ethanol. After this, the resultant mixtures were transferred to a corundum crucible and calcined at 1550 °C for 8 h under an air atmosphere in a high-temperature chamber furnace. After calcination, the samples were cooled down to room temperature in a furnace, and the samples were ground into powders for subsequent characterization.

### Structure and luminescence property characterization

The powder diffraction data of  $(\text{CaAl})_{1-x}(\text{YMg})_x\text{Al}_{11}\text{O}_{19}:\text{Mn}^{4+}$  for Rietveld analysis were obtained at room temperature using a Panalytical X'Pert powder diffractometer (Cu-K $\alpha$  radiation,  $\lambda = 0.15405$  nm) and a PIXcel 1d detector. The step size of  $2\theta$  was  $0.016^\circ$ , and the counting time was 2 s per step. The photoluminescence properties were detected using a Hitachi F-7000 fluorescence spectrophotometer equipped with a 150 W Xe lamp as the excitation source. The diffuse reflection (DR) spectrum was measured using Hitachi U4100 UV-VIS-NIR spectroscopy. The luminescence decay curves were measured *via* a Lecroy WaveRunner 6100 Digital Oscilloscope (1 GHz) using a tunable laser radiation (Nano-LED) as the excitation source. The photoluminescence quantum efficiency was detected directly using an Edinburgh FLS920 fluorescence spectrometer equipped with an integrating sphere. All the abovementioned measurements were performed at room temperature.

## Conclusions

In summary, red/far-red ratio-tunable  $\text{Mn}^{4+}$ -activated  $\text{Ca}_{1-x}\text{Y}_x\text{Al}_{12-x}\text{Mg}_x\text{O}_{19}$  ( $x = 0-0.50$ ) phosphors were prepared using a traditional solid-state reaction. The phase structures determined by X-ray diffraction and Rietveld refinement confirm the transformation mechanism of the composite compounds *via* the replacement of  $\text{Ca}^{2+}$  and  $\text{Al}^{3+}$  by  $\text{Y}^{3+}$  and  $\text{Mg}^{2+}$ , respectively. The refinement results indicated that the  $\text{Ca}_{1-x}\text{Y}_x\text{Al}_{12-x}\text{Mg}_x\text{O}_{19}$  ( $x = 0-0.50$ ) phase was composed of a predominant  $\text{CaAl}_{12}\text{O}_{19}$  phase accompanied by some impurity phases. The excitation spectra of the solid solution phosphors showed a broad absorption band covering the UV to the blue light region. Upon doping  $\text{Y}^{3+}$  and  $\text{Mg}^{2+}$  ions into the crystal lattice, a new peak emerged at 715 nm. The red/far-red ratio-tunable photoluminescence evolution was studied as a function of  $x$  in  $\text{Ca}_{1-x}\text{Y}_x\text{Al}_{12-x}\text{Mg}_x\text{O}_{19}$ . The emission of the phosphors can match well with the absorption spectrum of phytochrome (both  $\text{P}_R$  and  $\text{P}_{FR}$ ); this indicates that the as-prepared phosphors can be applied to obtain advanced plant growth LEDs. The absolute quantum yields of the  $\text{Y}^{3+}$  and  $\text{Mg}^{2+}$  co-substitution phosphors are higher than that of  $\text{CaAl}_{12}\text{O}_{19}$ . The abovementioned results demonstrate that  $\text{Ca}_{1-x}\text{Y}_x\text{Al}_{12-x}\text{Mg}_x\text{O}_{19}:\text{Mn}^{4+}$  are promising phosphors for plant growth LED applications.

## Conflicts of interest

There are no conflicts to declare.

## Acknowledgements

The present work was supported by the National Natural Science Foundation of China (Grant No. 21671070), the Project for Construction of High-level University in Guangdong Province, and the Teamwork Projects funded by the Guangdong Natural Science Foundation (Grant No. S2013030012842), and the Guangzhou Science & Technology Projects (No. 201704030086, 201605030005), and the reported study was funded by the RFBR according to the research project 17-52-53031. Special Funds for the Cultivation of Guangdong College Students' Scientific and Technological Innovation ("Climbing Program" Special Funds) were granted for Dr Yinjian Zheng.

## Notes and references

- 1 C. D'Souza, H. Yuk, G. Khoo and W. Zhou, *Compr. Rev. Food Sci. Food Saf.*, 2015, **14**, 719.
- 2 Z. Bian, Q. Yang and W. Liu, *J. Sci. Food Agric.*, 2015, **95**, 869.
- 3 A. Yano and K. Fujiwara, *Plant Methods*, 2012, **8**, 46.
- 4 G. Massa, H. Kim, R. Wheeler and C. Mitchell, *Hortscience*, 2008, **43**, 1951.
- 5 N. Yeh and J. Chung, *Renewable Sustainable Energy Rev.*, 2009, **13**, 2175.
- 6 M. Olle and A. Viršile, *Agric. Food Sci.*, 2013, **22**, 223.
- 7 D. Patel, M. Basu, S. Hayes and I. Majláth, *Plant J.*, 2013, **73**, 980.
- 8 Y. Hori, K. Nishidate, M. Nishiyama, K. Kanahama and Y. Kanayama, *Planta*, 2011, **234**, 321.
- 9 Y. Park and E. Runkle, *Acta Hort.*, 2016, **1134**, 259.
- 10 B. Prasad, S. Kumar, A. Nandi and S. Chattopadhyay, *BMC Plant Biol.*, 2012, **12**, 37.
- 11 P. Quail, *Nat. Rev. Mol. Cell Biol.*, 2002, **3**, 85.
- 12 J. Sullivan and X. Deng, *Dev. Biol.*, 2003, **260**, 289.
- 13 J. Chen, N. Zhang, C. Guo, F. Pan, X. Zhou, H. Suo, X. Zhao and E. Goldys, *ACS Appl. Mater. Interfaces*, 2016, **8**, 20856.
- 14 A. Agarwal and S. Gupta, *Curr. Biotechnol.*, 2016, **5**, 28.
- 15 Z. Zhou, J. Zheng, R. Shi, N. Zhang, J. Chen, R. Zhang, H. Suo, E. Goldys and C. Guo, *ACS Appl. Mater. Interfaces*, 2017, **9**, 6177.
- 16 L. Cao, Q. Lu, L. Wang, J. Li, J. Song and D. Wang, *Ceram. Int.*, 2013, **39**, 7717.
- 17 Q. Lu, J. Li and D. Wang, *ECS Solid State Lett.*, 2012, **1**, 24.
- 18 Q. Lu, J. Li and D. Wang, *Curr. Appl. Phys.*, 2013, **13**, 1506.
- 19 L. Ma, D. Wang, Z. Mao, Q. Lu and Z. Yuan, *Appl. Phys. Lett.*, 2008, **93**, 144101.
- 20 Y. Zhang, Z. Mao, D. Wang and J. Zhao, *Mater. Res. Bull.*, 2015, **67**, 1.
- 21 J. Chen, C. Guo, Z. Yang, T. Li, J. Zhao and J. McKittrick, *J. Am. Ceram. Soc.*, 2016, **99**, 218.
- 22 Z. Pan, Y. Xu, Q. Hu, W. Li, H. Zhou and Y. Zheng, *RSC Adv.*, 2015, **5**, 9489.
- 23 Z. Pan, W. Li, Y. Xu, Q. Hua and Y. Zheng, *RSC Adv.*, 2016, **6**, 20458.
- 24 Z. Zhou, J. Zheng, R. Shi, N. Zhang, J. Chen, R. Zhang, H. Suo, E. Goldys and C. Guo, *ACS Appl. Mater. Interfaces*, 2017, **9**, 6177.
- 25 M. Brik and A. Srivastava, *J. Lumin.*, 2013, **133**, 69.
- 26 T. Murata, T. Tanoue, M. Iwasaki, K. Morinaga and T. Hase, *J. Lumin.*, 2005, **114**, 207.
- 27 M. Brik, Y. Pan and G. Liu, *J. Alloys Compd.*, 2011, **509**, 1452.
- 28 Y. Pan and G. Liu, *J. Lumin.*, 2011, **131**, 465.
- 29 W. Shu, L. Jiang, S. Xiao, X. Yang and J. Ding, *Mater. Sci. Eng. B*, 2012, **177**, 274.
- 30 J. Lu, Y. Pan, J. Wang, X. Chen, S. Huang and G. Liu, *RSC Adv.*, 2013, **3**, 4510.
- 31 H. Ji, L. Wang, M. Molokeev, N. Hirotsaki, Z. Huang, Z. Xia, M. Otmar, L. Liu and R. Xie, *J. Mater. Chem. C*, 2016, **4**, 2359.
- 32 C. Liu, Z. Xia, M. Chen, M. Molokeev and Q. Liu, *Inorg. Chem.*, 2015, **54**, 1876.
- 33 Z. Xia, M. Molokeev, W. Im, S. Unithrattil and Q. Liu, *J. Phys. Chem. C*, 2015, **119**, 9488.
- 34 S. Wang, W. Chen, Y. Li, J. Wang and H. She, *J. Am. Chem. Soc.*, 2013, **135**, 12504.
- 35 Z. Xia, C. Ma, M. Molokeev, Q. Liu, K. Rickert and K. Poepplmeier, *J. Am. Chem. Soc.*, 2015, **137**, 12494.
- 36 Y. Xia, J. Chen, Y. Liu, M. Molokeev, M. Guan, Z. Huang and M. Fang, *Dalton Trans.*, 2016, **45**, 1007.
- 37 Bruker AXS TOPAS V4: General Profile and Structure Analysis Software for Powder Diffraction Data. User's Manual. Bruker AXS, Karlsruhe, Germany, 2008.
- 38 K. Kato and H. Saalfeld, *Neues Jahrb. Mineral., Abh.*, 1968, **109**, 192.
- 39 Z. Xia, M. Molokeev, W. Im, S. Unithrattil and Q. Liu, *J. Phys. Chem. C*, 2015, **119**, 9488.
- 40 M. Brik, S. Camardello and A. Srivastava, *ECS J. Solid State Sci. Technol.*, 2014, **4**, 39.
- 41 V. Singh, R. Chakradhar, J. Rao and D. Kim, *J. Solid State Chem.*, 2007, **180**, 2067.
- 42 M. Noginov and G. Loutts, *J. Opt. Soc. Am. B*, 1999, **16**, 3.
- 43 Y. Zhydachevskii, D. Galanciak, S. Kobayakov, M. Berkowski, A. Kamińska, A. Suchocki, Y. Zakharko and A. Durygin, *J. Phys.: Condens. Matter*, 2006, **18**, 11385.
- 44 B. Jovani, *J. Lumin.*, 1997, **75**, 171.
- 45 Z. Xia, G. Liu, J. Wen, Z. Mei, M. Balasubramanian, M. Molokeev, L. Peng, L. Gu, D. Miller, Q. Liu and K. Poepplmeier, *J. Am. Chem. Soc.*, 2016, **138**, 1158.
- 46 G. Zhu, Z. Ci, Q. Wang, Y. Wen and S. Han, *J. Mater. Chem. C*, 2013, **1**, 4490.
- 47 L. Liu, M. Yu, J. Zhang, B. Wang and W. Liu, *J. Mater. Chem. C*, 2015, **3**, 2326.
- 48 R. Cao, K. Sharafudeen and J. Qiu, *Spectrochim. Acta, Part A*, 2014, **117**, 402.